JOURNAL OF COMPUTATIONAL PHYSICS **145,** 89–109 (1998)
ARTICLE NO. CP986014

Fictitious Domain Methods for the Numerical Solution of Two-Dimensional Scattering Problems[1]

Erkki Heikkola,*,[2] Yuri A. Kuznetsov,† Pekka Neittaanmäki,* and Jari Toivanen*

Laboratory of Scientific Computing, Department of Mathematics, University of Jyväskylä, P.O. Box 35, FIN–40351 Jyväskylä, Finland; and †Department of Mathematics, University of Houston, 4800 Calhoun Road, Houston, Texas 77204–3476

Received November 25, 1996; revised April 20, 1998

Fictitious domain methods for the numerical solution of two-dimensional scattering problems are considered. The original exterior boundary value problem is approximated by truncating the unbounded domain and by imposing a nonreflecting boundary condition on the artificial boundary. First-order, second-order, and exact nonreflecting boundary conditions are tested on rectangular and circular boundaries. The finite element discretizations of the corresponding approximate boundary value problems are performed using locally fitted meshes, and the discrete equations are solved with fictitious domain methods. A special finite element method using nonmatching meshes is considered. This method uses the macro-hybrid formulation based on domain decomposition to couple polar and cartesian coordinate systems. A special preconditioner based on fictitious domains is introduced for the arising algebraic saddle-point system such that the subspace of constraints becomes invariant with respect to the preconditioned iterative procedure. The performance of the new method is compared to the fictitious domain methods both with respect to accuracy and computational cost.

Key Words: acoustic scattering; nonreflecting boundary conditions; fictitious domain methods; macro-hybrid formulation; domain decomposition; nonmatching meshes.

1. INTRODUCTION

In this article, we consider the two-dimensional exterior Helmholtz equation,

$$\Delta u + \omega^2 u = 0 \qquad \text{in } \mathbb{R}^2 \backslash \bar{\Omega}, \tag{1.1a}$$

[1] This research was partially supported by Academy of Finland Grant 34063.

[2] Corresponding author. E-mail: emsh@math.jyu.fi.

0021-9991/98 $25.00

$$u = -v_I \quad \text{on } \partial\Omega, \tag{1.1b}$$

$$\lim_{r\to\infty} \sqrt{r}\left(\frac{\partial u}{\partial r} - \mathbf{i}\omega u\right) = 0, \tag{1.1c}$$

which can be used to model the scattering of time-harmonic electromagnetic or acoustic waves by an obstacle denoted by Ω. Here, $v_I(\mathbf{x}) = e^{i\omega\cdot\mathbf{x}}$ is the time-harmonic incident plane wave the direction of propagation of which is given by the vector $\boldsymbol{\omega}$. The well-posedness of the boundary value problem (1.1) is considered, for example, in [1].

Numerical solution of scattering problems has aroused active research interest, because efficient methods would facilitate the simulation of many important physical phenomena in underwater acoustics, medicine, and radar technology, for example. In electromagnetic wave simulations, the frequency of the wave motion is usually high, which creates problems in the efficient and accurate solution of the associated equations. When the frequency is increased, either the computational cost or the memory consumption become the bottlenecks, and it is necessary to develop special techniques to reduce these factors.

The standard approaches for the numerical solution of scattering problems are the finite element method with unstructured meshes and the boundary element method. The finite element method leads to a sparse and conveniently structured system of linear equations to be solved, but to obtain reasonable accuracy it is necessary to have a very dense discretization mesh inside the computational domain. Thus, the arising linear system involves a large number of equations the solution of which requires extensive computer capacity. The boundary element methods, on the other hand, result in fewer equations to be solved, because only the boundary of the obstacle needs to be discretized. However, the coefficient matrix of the linear system of equations is dense and does not, in general possess any special structure. Iterative solution requires matrix–vector multiplications with this dense coefficient matrix on each iteration step, and the computational cost of this operation is $\mathcal{O}(n^2)$, where n is the number of nodes on the boundary. Therefore, also in this case the memory and CPU time consumptions become large. The cost of the multiplication can be significantly reduced by using the fast multipole method, which provides an efficient way to compute (with given accuracy) the matrix–vector multiplication [2]. The boundary element methods, together with the fast multipole method comprise a very efficient and attractive approach to solve scattering problems.

Fictitious domain methods with separable preconditioners are efficient solution algorithms for elliptic mesh equations arising from finite element (or finite difference) discretization (see, e.g., [3, 4]), and they have been applied succesfully also to the exterior Helmholtz problem [5, 8, 9, 12]. In this paper, we concentrate on this methodology and consider its efficient application to the numerical solution of the two-dimensional Helmholtz equation in (1.1). The algebraic fictitious domain methods are closely related to, and often coincide with, the capacitance matrix methods the application of which to scattering problems is considered in [13].

We consider also the macro-hybrid formulation-based domain decomposition for the boundary value problem in (1.1), which was first considered by Goldstein in [15]. This formulation is used to couple polar and cartesian coordinate systems by partitioning the computational domain into two parts and by constructing polar and cartesian meshes in the two subdomains. These meshes become nonmatching on the subdomain interface, and the solutions in the two subregions are glued together by a weak continuity condition. Discretization leads to a saddle-point linear system, which is preconditioned with a special

matrix based on fictitious domains. It turns out that the subspace of constraints becomes invariant with respect to the corresponding preconditioned iterative procedure.

The rest of the paper is organized as follows: In Section 2, we consider different nonreflecting boundary conditions and the corresponding approximate boundary value problems. Furthermore, we give some motivations for the numerical tests presented in this article. In Section 3, we describe the fictitious domain method and its implementation, while the coupling of the two coordinate systems is considered in Section 4. In Section 5, we describe the computation of the radar cross sections of the numerical solutions, and in Section 6, we present the test examples we have used to compare the different methods. Section 7 is devoted to the results of several numerical experiments the purpose of which is to study the accuracy of the different nonreflecting boundary conditions and to compare the accuracy and efficiency of the new finite element method using nonmatching meshes to the fictitious domain methods working with matching meshes.

2. APPROXIMATE BOUNDARY VALUE PROBLEMS

We approximate the original problem (1.1) by truncating the unbounded domain with an artificial boundary, denoted by Γ_∞, and by introducing an intermediate boundary value problem in the arising bounded domain. The shape of the artificial boundary depends on the underlying coordinate system such that in polar coordinates it is a circle of radius R, while in cartesian coordinates it is a rectangle of width D (see Fig. 1). The aim is to choose the boundary condition on Γ_∞ such that the solution of the intermediate problem gives a good approximation to the solution of the original exterior problem within the computational domain $\Pi\backslash\bar{\Omega}$. For a review on different nonreflecting boundary conditions for the Helmholtz equation see [16, 17]. The error caused by the truncation of the domain has been analyzed, for example, in [14, 18, 20, 21].

In general, the approximate boundary value problem is of the form

$$\Delta u + \omega^2 u = 0 \qquad \text{in } \Pi\backslash\bar{\Omega}, \tag{2.1a}$$

$$u = -v_I \quad \text{on } \partial\Omega, \tag{2.1b}$$

$$\mathcal{M}u = 0 \qquad \text{on } \Gamma_\infty, \tag{2.1c}$$

where the operator $\mathcal{M}$ corresponds to the chosen boundary condition. On a circular boundary, we use the first-order and second-order nonreflecting boundary conditions introduced

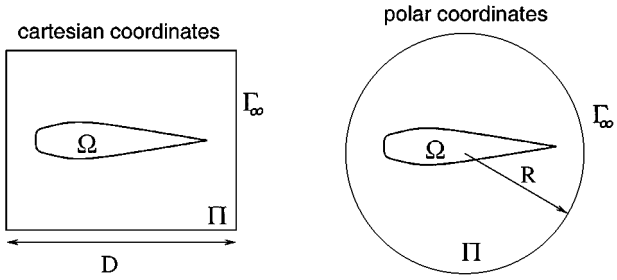

FIG. 1. The rectangular and circular artificial boundaries.

by Engquist and Majda [19]. The operators $\mathcal{M}$ corresponding to these two conditions are given by

$$\mathcal{M} \equiv \frac{\partial}{\partial r} - \left(\mathbf{i}\omega - \frac{1}{2R}\right) \tag{2.2}$$

and

$$\mathcal{M} \equiv \frac{\partial}{\partial r} - \left(\mathbf{i}\omega - \frac{1}{2R}\right) - \left(\frac{\mathbf{i}}{2\omega R^2} + \frac{1}{2\omega^2 R^3}\right)\frac{\partial^2}{\partial\theta^2}, \tag{2.3}$$

respectively. On a rectangular boundary, the standard first-order nonreflecting boundary condition is given by

$$\mathcal{M}u \equiv \frac{\partial u}{\partial \mathbf{n}} - \mathbf{i}\omega u = 0. \tag{2.4}$$

We use also the second-order boundary condition, which contains additional conditions on the corners of the boundary [22]:

$$\begin{aligned} \frac{\partial u}{\partial \mathbf{n}} - \mathbf{i}\omega u - \frac{\mathbf{i}}{2\omega}\frac{\partial^2 u}{\partial \mathbf{s}^2} = 0 \qquad & \text{on } \Gamma_\infty, \\ \pm\frac{\partial u}{\partial x_1} \pm \frac{\partial u}{\partial x_2} = \mathbf{i}\frac{3}{2}\omega u \quad & \text{on } C. \end{aligned} \tag{2.5}$$

Here, C denotes the set of corner points of the rectangular boundary and $\mathbf{s}$ is the unit vector, which is tangential to the rectangle boundary. The signs in the corner condition are chosen such that the derivatives are directed outward.

The exact nonreflecting boundary condition on a circular boundary is given by

$$\frac{\partial u}{\partial r} = Mu \equiv \frac{\omega}{\pi} \cdot {\sum_{n=0}^{\infty}}' \frac{H_n^{(1)'}(\omega R)}{H_n^{(1)}(\omega R)} \int_0^{2\pi} \cos(n(\theta - \theta'))u(R, \theta')\, d\theta', \tag{2.6}$$

where M denotes the Dirichlet-to-Neumann (DtN) mapping, which relates the Dirichlet and Neumann data of this particular problem [23, 24]. The summation symbol with a prime means that the first term in the sum is divided by two. In numerical computations, we are able to use only a finite number of terms in (2.6), which leads to an approximate DtN operator M^K. In [25], a lower bound for K is derived to guarantee the unique solvability of the new problem. Our algorithm allows us to take a large number of terms without significantly affecting the computational cost, because the computation of the necessary matrix components is a preprocessing stage requiring only $\mathcal{O}(K)$ operations (see Section 3).

The main difference between the boundary value problems in rectangular and circular domains is the direction of the first-order derivative in the nonreflecting boundary conditions. This direction is normal to the boundary Γ_∞, which, in the case of a circular boundary, is the radial direction. It has been shown that with the nonreflecting boundary conditions (2.2) and (2.3), it is possible to reach any accuracy by increasing the radius R of the artificial boundary and the discretization accuracy [14, 18].

We introduce the function spaces V^f and V^s by

$$V^f \equiv H^1(\Pi\backslash\Omega), \quad V^s \equiv \left\{v \in V^f : v|_{\Gamma_\infty} \in H^1(\Gamma_\infty)\right\} \tag{2.7}$$

and the spaces $V^{f,0}$ and $V^{s,0}$ by

$$V^{f,0} \equiv \{v \in V^f : v|_{\partial\Omega} = 0\}, \quad V^{s,0} \equiv \{v \in V^s : v|_{\partial\Omega} = 0\}. \tag{2.8}$$

Let the function $\hat{g} \in V^f$ be such that $\text{trace}|_{\partial\Omega}\hat{g} = -v_I \in H^{1/2}(\partial\Omega)$ and that supp $\hat{g} \subset \Pi\backslash\Omega$. Then, the weak formulation of the boundary value problem (2.1) is: Find $u \in V$ such that $u - \hat{g} \in V^0$ and

$$a(u, v) = 0 \quad \forall v \in V^0, \tag{2.9}$$

where $a(\cdot, \cdot)$ is the bilinear form associated with the boundary value problem. In the case with the first-order or exact boundary conditions, the spaces V and V^0 are given by V^f and $V^{f,0}$. The second-order conditions (2.3) and (2.5) require additional regularity on the boundary Γ_∞, which is provided by the spaces V^s and $V^{s,0}$.

The bilinear forms $a(\cdot, \cdot)$ corresponding to the first-order, second-order, and exact boundary conditions (2.2), (2.3), and (2.6), respectively, are given by

$$a_f(u, v) = \int_{\Pi\backslash\Omega} \left(r \frac{\partial u}{\partial r} \frac{\partial \bar{v}}{\partial r} + \frac{1}{r} \frac{\partial u}{\partial \theta} \frac{\partial \bar{v}}{\partial \theta} - \omega^2 r u \bar{v} \right) dx - \left(\mathbf{i}\omega - \frac{1}{2R} \right) \int_{\Gamma_\infty} u \bar{v}\, ds, \tag{2.10}$$

$$a_s(u, v) = a_f(u, v) + \left(\frac{\mathbf{i}}{2\omega R^2} + \frac{1}{2\omega^2 R^3} \right) \int_{\Gamma_\infty} \frac{\partial u}{\partial \theta} \frac{\partial \bar{v}}{\partial \theta}\, d\theta, \tag{2.11}$$

and

$$a_e(u, v) = \int_{\Pi\backslash\Omega} \left(r \frac{\partial u}{\partial r} \frac{\partial \bar{v}}{\partial r} + \frac{1}{r} \frac{\partial u}{\partial \theta} \frac{\partial \bar{v}}{\partial \theta} - \omega^2 r u \bar{v} \right) dx - \int_{\Gamma_\infty} M^K u \bar{v}\, ds, \tag{2.12}$$

respectively.

In the case of a rectangular boundary, the bilinear forms corresponding to the first-order and second-order boundary conditions (2.4) and (2.5), respectively, are given by

$$a_f(u, v) = \int_{\Pi\backslash\Omega} (\nabla u \cdot \nabla \bar{v} - \omega^2 u \bar{v})\, dx - \mathbf{i}\omega \int_{\Gamma_\infty} u \bar{v}\, ds \tag{2.13}$$

and

$$a_s(u, v) = a_f(u, v) + \frac{\mathbf{i}}{2\omega} \int_{\Gamma_\infty} \frac{\partial u}{\partial \mathbf{s}} \frac{\partial \bar{v}}{\partial \mathbf{s}}\, ds + \frac{3}{4} \sum_{\mathbf{x} \in C} u(\mathbf{x}) \bar{v}(\mathbf{x}), \tag{2.14}$$

respectively.

The finite element discretization of the problem (2.9) is based on a locally fitted mesh, which is obtained from an orthogonal cartesian or polar mesh, denoted by Π_h, inside the domain Π. The nodes of the mesh, which are next to the boundary of obstacle Ω are shifted onto the boundary curve $\partial\Omega$, and the modified elements are triangulated such that the resulting mesh gives a second-order approximation to the shape of the obstacle. This leads to the locally fitted mesh, which is topologically equivalent to the original mesh and differs from it only in an h–neighbourhood of the obstacle boundary (see, e.g., [6]). The restriction of the locally fitted mesh into the domain $\Pi\backslash\bar{\Omega}$ is denoted by Ω_h and the mesh on the boundary $\partial\Omega$ by σ_h. The generation of a locally fitted mesh is illustrated in Fig. 2.

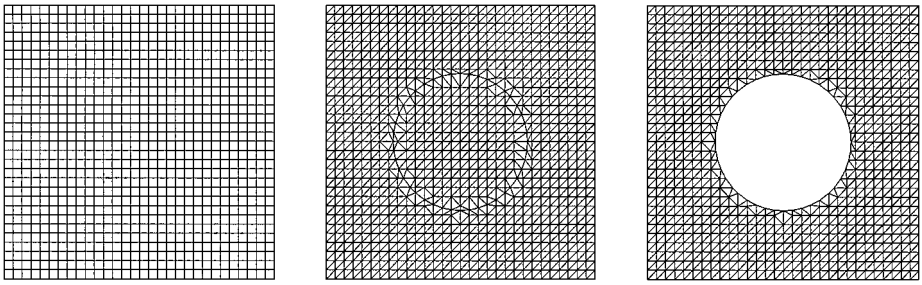

FIG. 2. An initial grid Π_h, the locally fitted mesh, and the mesh Ω_h.

It is well known that the accuracy of the finite element discretization of the Helmholtz equation deteriorates with increasing wave number ω [26]. The finite element solution satisfies a quasioptimal error estimate only under the assumption $\omega^2 h = \mathcal{O}(1)$, where h is the mesh parameter. Under the assumption $\omega h = \mathcal{O}(1)$, the finite element approximation involves, in addition to the error of the best approximation, a pollution term, whose magnitude is $\mathcal{O}(\omega^3 h^2)$. This term becomes significant for large wave numbers ω, which limits the applicability of finite element methods in high-frequency problems.

Based on the element partitioning of the domain $\Pi \backslash \bar{\Omega}$, we introduce the standard piecewise linear finite element spaces V_h and V_h^0 corresponding to the spaces V and V^0 in (2.9). The finite element problem is then: Find $u_h \in V_h$, $u_h = g_h$ on $\partial\Omega_h$, such that

$$a(u_h, v_h) = 0 \quad \forall v_h \in V_h^0. \tag{2.15}$$

Here, the function $g_h \in V_h$ is the piecewise linear interpolate of the function $-v_I$. Problem (2.15) can be represented as a linear system of equations

$$\mathbf{A}_1 \mathbf{u}_1 = \mathbf{f}, \tag{2.16}$$

where $\mathbf{A}_1$ is a complex symmetric matrix. We remark that mass lumping is applied in the computation of the matrix elements.

3. ALGEBRAIC FICTITIOUS DOMAIN METHODS

3.1. *Enlargement of the Original System*

The basic idea of the algebraic fictitious domain methodology is to replace the original linear system of algebraic equations (2.16) by an equivalent, but enlarged, system of equations

$$\hat{\mathbf{A}}\hat{\mathbf{u}} = \hat{\mathbf{f}} \equiv \begin{pmatrix} \mathbf{f} \\ \mathbf{0} \end{pmatrix}, \quad \hat{\mathbf{A}} \in \mathbb{C}^{N \times N},\ N > n. \tag{3.1}$$

These two systems are required to be equivalent in the sense that the solution vector $\mathbf{u}$ should be obtained as the first block of the vector $\hat{\mathbf{u}}$ [3]. The benefit of this approach is that there are wider possibilities to construct efficient preconditioners for the enlarged system (3.1) than for the original one.

In this paper, we consider enlargements of the form

$$\hat{\mathbf{A}} \equiv \begin{pmatrix} \mathbf{A}_1 & \mathbf{A}_{12} \\ \mathbf{0} & \mathbf{A}_2 \end{pmatrix}, \tag{3.2}$$

where $\ker \mathbf{A}_2 \subseteq \ker \mathbf{A}_{12}$, and thereby the first block of the solution $\hat{\mathbf{u}}$ to the system (3.1) solves the original system (2.16). The enlarged matrix $\hat{\mathbf{A}}$ may be chosen to be singular in which case the iterative solution is implemented with respect to an appropriate subspace (see Section 3.2). In fact, in the numerical experiments, we use the enlargement given by $\mathbf{A}_{12} = \mathbf{0}$ and $\mathbf{A}_2 = \mathbf{0}$, which is called the zero-enlargement.

The preconditioner, denoted by $\mathbf{B}$, is introduced for the enlarged system and can be written in the block form

$$\mathbf{B} \equiv \begin{pmatrix} \mathbf{B}_1 & \mathbf{B}_{12} \\ \mathbf{B}_{21} & \mathbf{B}_2 \end{pmatrix}. \tag{3.3}$$

The enlargement of the original system and the construction of the preconditioner $\mathbf{B}$ are usually based on embedding the original bounded domain into a larger domain Π, which has a simple shape (e.g., rectangle or circle). Then, the matrix $\mathbf{B}$ corresponds to the Helmholtz operator in the domain Π.

3.2. *Iterative Methods in Subspaces*

The algebraic fictitious domain methods can often be realized in a subspace, whose dimension is lower by an order of magnitude compared to the dimension of the original system. This fact is significant in view of memory consumption and can be utilized to improve the computational efficiency. Matrix iterative methods in subspaces are considered in a general setting, for example, in [7].

Here, we apply preconditioned iterative methods of the form

$$\mathbf{B}(\mathbf{u}^p - \mathbf{u}^{p-1}) = -\sum_{i=0}^{p-1} \tau_{p,i}(\hat{\mathbf{A}}\mathbf{u}^i - \hat{\mathbf{f}}), \quad p > 0. \tag{3.4}$$

The initial approximation $\mathbf{u}^0$ is introduced by the equation

$$\mathbf{B}(\mathbf{u}^0 - \mathbf{w}) = -(\hat{\mathbf{A}}\mathbf{w} - \hat{\mathbf{f}}), \tag{3.5}$$

where $\mathbf{w}$ is an arbitrary vector. Then, the initial residual vector $\mathbf{r}^0$,

$$\mathbf{r}^0 \equiv \hat{\mathbf{A}}\mathbf{u}^0 - \hat{\mathbf{f}} = (\mathbf{I} - \hat{\mathbf{A}}\mathbf{B}^{-1})(\hat{\mathbf{A}}\mathbf{w} - \hat{\mathbf{f}}), \tag{3.6}$$

belongs to the subspace

$$U_{\mathbf{A}} \equiv \operatorname{im}[(\mathbf{I} - \hat{\mathbf{A}}\mathbf{B}^{-1})\hat{\mathbf{A}}] = \operatorname{im}\hat{\mathbf{A}} \cap \operatorname{im}(\mathbf{B} - \mathbf{A}), \tag{3.7}$$

and it is easy to see that the subspace $U_{\mathbf{A}}$ is invariant with respect to the method (3.4), that is, $\mathbf{r}^p \in U_{\mathbf{A}}$ for all $p \geq 0$.

If most of the rows of the matrices $\hat{\mathbf{A}}$ and $\mathbf{B}$ coincide, the subspace $U_{\mathbf{A}}$ obviously has a low dimension and, consequently, the residual vectors $\mathbf{r}^p$ have only a few nonzero components.

In this case, we are able to realize the iterative process (3.4) in a low dimensional subspace of $\mathbb{R}^N$. This fact motivates the use of locally fitted meshes in the finite element discretization, because we are then able to introduce a separable preconditioner $\mathbf{B}$ such that most of the rows of the matrix $\mathbf{C} \equiv \hat{\mathbf{A}} - \mathbf{B}$ are equal to zero. In the two-dimensional case considered in this paper, the vectors in the corresponding space $U_{\mathbf{A}}$ have typically $\mathcal{O}(\sqrt{N})$ nonzero elements.

Furthermore, the sparse structure of the vectors provides the possibility to apply the partial solution method, which is a special implementation of the standard method of separation of variables, to the linear systems with the separable preconditioner [27, 10]. Standard fast direct methods for such linear systems require $\mathcal{O}(N \log N)$ arithmetical operations, but the partial solution method reduces the cost to $\mathcal{O}(N)$ operations.

3.3. *Construction of the Preconditioner*

Here, we introduce the separable fictitious domain preconditioner, denoted by $\mathbf{B}$, which corresponds to the Helmholtz equation with a nonreflecting boundary condition in the rectangular or circular domain Π:

$$\Delta u(\mathbf{x}) + \omega^2 u(\mathbf{x}) = 0, \quad \mathbf{x} \in \Pi, \tag{3.8a}$$

$$\mathcal{M} u(\mathbf{x}) = 0, \quad \mathbf{x} \in \Gamma_\infty. \tag{3.8b}$$

The preconditioner $\mathbf{B}$ is obtained by finite element discretization of the problem (3.8) using the original orthogonal mesh Π_h. Discretization using piecewise linear finite elements with mass lumping leads to a separable matrix; that is, it can be represented in the tensor product form

$$\mathbf{B} = \mathbf{M}_2 \otimes \mathbf{A}_1 + \mathbf{A}_2 \otimes \mathbf{M}_1 - \omega^2 \mathbf{M}_2 \otimes \hat{\mathbf{M}}_1 - \left(\mathbf{D} \otimes \mathbf{e}_{n_1}^{n_1} \mathbf{e}_{n_1}^{n_1 T}\right) \tag{3.9}$$

with the tridiagonal matrices $\mathbf{A}_i \in \mathbb{C}^{n_i}$ and diagonal matrices $\mathbf{M}_i \in \mathbb{C}^{n_i}$ and $\hat{\mathbf{M}}_1 \in \mathbb{C}^{n_i}$, $i = 1, 2$, where n_1 and n_2 are the number of nodes in the two coordinate directions. The matrix $\mathbf{D}$ is included in the representation (3.9) only in the case of a circular artificial boundary, and it corresponds to the nonreflecting boundary condition. The vector $\mathbf{e}_i^n$ denotes the usual ith canonical basis vector of $\mathbb{R}^n$.

If we use the local first-order boundary condition (2.2) or the second-order condition (2.3), the matrix $\mathbf{D}$ becomes a tridiagonal matrix and can be written as a linear combination,

$$\mathbf{D} = c_1 \mathbf{M}_2 + c_2 \mathbf{A}_2, \quad c_1, c_2 \in \mathbb{C}. \tag{3.10}$$

On the other hand, the exact condition (2.6) results in a dense block of the form

$$\mathbf{D} = \frac{\omega R}{\pi} \cdot \sum_{n=0}^{K} \alpha_n \gamma_n \mathbf{C}_n, \tag{3.11}$$

with circulant matrices $\mathbf{C}_n$. Explicit forms of these matrices, as well as values for the coefficients α_n and γ_n, can be found, for example, in [13].

Fast solution methods based on separation of variables for linear systems with separable matrices are well known. Such fast solvers are available also in the case of the exact nonreflecting boundary condition, because the Fourier matrix diagonalizes the dense matrix $\mathbf{D}$ in (3.11) [13].

4. COUPLING OF COORDINATE SYSTEMS

In this section, we consider the macro-hybrid formulation based on domain decomposition for the boundary value problem (2.1). To our knowledge, the application of this formulation to the numerical solution of the Helmholtz equation was first considered by Goldstein in [15]. The hybrid formulation allows the introduction of independent discretization meshes in different subdomains, and here we use it to couple polar and cartesian coordinate systems [11].

The coupling is based on dividing the computational domain into two subdomains, G_1 and G_2, with a circular interface Γ of radius R_Γ. Then, polar coordinates are employed in the subdomain G_1, while cartesian ones are used in the domain G_2 (see Fig. 3). The choice of the coordinate systems is motivated by the distribution of nodes in orthogonal grids associated with the two coordinate systems: A polar grid is convenient for approximating the asymptotic behaviour of the scattered wave, but it becomes unnecessarily dense near the origin of coordinates, which increases the dimension of the linear system arising from discretization. Therefore, a natural idea is to use cartesian grid within the domain G_2, while having an orthogonal polar grid in the outer domain G_1. For simplicity, we impose the first-order nonreflecting boundary condition (2.2) on Γ_∞, but also the second-order and exact conditions may be used in a similar manner.

We introduce three function spaces V, Y, and Λ by

$$V \equiv H^1(G_1) \times H^1(G_2), \quad Y \equiv H^1(G_1) \times V_2^0, \quad \Lambda \equiv H^{-1/2}(\Gamma), \tag{4.1}$$

where the space V_2^0 is given by

$$V_2^0 \equiv \left\{ v \in H^1(G_2) : v|_{\partial\Omega} = 0 \right\}. \tag{4.2}$$

The bilinear forms $a_1(\cdot,\cdot)$ and $a_2(\cdot,\cdot)$ on $V \times V$ are given by $a_1(u, v) \equiv a_f(u_1, v_1)$ and

$$a_2(u, v) \equiv \int_{G_2} \left(\nabla u_2 \cdot \nabla \bar{v}_2 - \omega^2 u_2 \bar{v}_2 \right), \tag{4.3}$$

respectively. Then, the form $a(\cdot,\cdot)$ is introduced by summarizing a_1 and a_2, $a(\cdot,\cdot) \equiv a_1(\cdot,\cdot) + a_2(\cdot,\cdot)$.

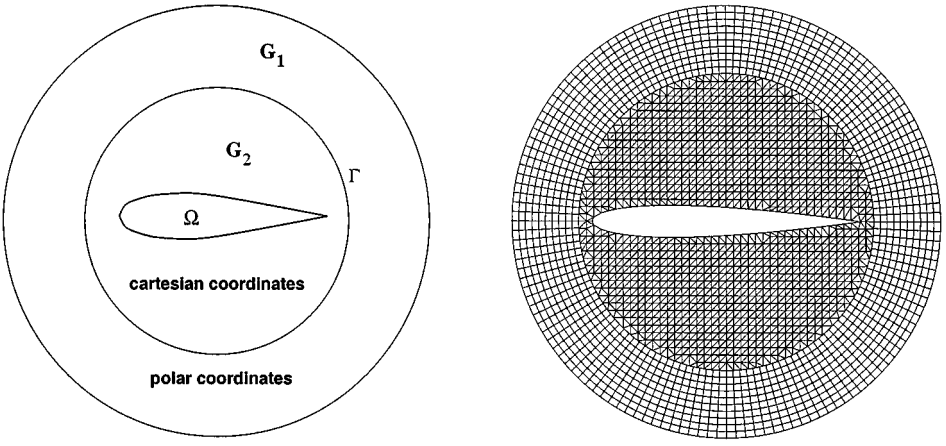

FIG. 3. Partitioning of the domain into subdomains, and their discretization with nonmatching grids.

We introduce a function $g_2 \in V_2$ such that $\text{trace}|_{\partial\Omega} g_2 = -v_I$. Then, the macro-hybrid formulation of Eq. (2.1) is: Find $(\mathbf{u}, \lambda) \in V \times \Lambda$, $u_2 - g_2 \in V_2^0$, such that

$$a(\mathbf{u}, \mathbf{v}) + b(\lambda, \mathbf{v}) = 0 \quad \forall \mathbf{v} \in Y, \tag{4.4a}$$

$$b(\mu, \mathbf{u}) = 0 \quad \forall \mu \in \Lambda. \tag{4.4b}$$

Here, $b(\mu, \mathbf{u}) \equiv \langle \mu, u_1 \rangle_\Gamma - \langle \mu, u_2 \rangle_\Gamma$ and, hence, the second equation in (4.4) guarantees the weak continuity of u over Γ.

There are no constraints on the components of V with respect to the interface Γ, which allows us to use independent meshes inside the two subdomains. In the annulus G_1, we introduce a uniform orthogonal polar mesh, denoted by $G_{1,h}$. To generate the mesh in the domain G_2, we first embed it into a rectangle $\hat{\Pi}$ and construct an orthogonal triangular mesh $\hat{\Pi}_h$ inside the rectangle. This mesh is then locally deformed according to the boundary of the obstacle and to the circle Γ, which leads to the locally fitted mesh $G_{2,h}$ (see Fig. 3). Thus, we obtain piecewise linear approximations σ_h and Γ_h to the boundaries $\partial\Omega$ and Γ, respectively.

We introduce the standard piecewise bilinear finite element space $V_{1,h}$ corresponding to the polar mesh $G_{1,h}$ and the piecewise linear finite element space $V_{2,h}$ corresponding to the locally fitted triangular mesh $G_{2,h}$. The vector spaces V_h and Y_h corresponding to the spaces V and Y from (4.1) are then given by

$$V_h \equiv V_{1,h} \times V_{2,h}, \quad Y_h \equiv V_{1,h} \times V_{2,h}^0. \tag{4.5}$$

The approximation space Λ_h for the Lagrange multipliers is chosen to be the restriction of the finite element space $V_{1,h}$ to the interface Γ:

$$\Lambda_h \equiv \text{trace}|_\Gamma V_{1,h} \equiv \{\lambda_h : \exists v_{1,h} \in V_{1,h}, \lambda_h = v_{1,h}|_\Gamma\}. \tag{4.6}$$

Because functions $v_{2,h} \in V_{2,h}$ are not defined on the interface Γ, but on its piecewise linear approximation, $b(\lambda, \mathbf{v})$ is not defined for $\mathbf{v} \in V_h$. Therefore, to obtain a properly defined finite element problem, we need to modify the bilinear form $b(\cdot, \cdot)$. For this purpose, we introduce a transformation operator T, which maps a function $v : \Gamma_h \to \mathbb{R}$, which is piecewise linear with respect to the cartesian coordinates, into a function $Tv : \Gamma \to \mathbb{R}$, which is piecewise linear with respect to the polar coordinates, such that the nodal values remain unchanged; that is,

$$v(\mathbf{x}) = Tv(\mathbf{x}) \quad \forall \mathbf{x} \in \Gamma \cap \Gamma_h. \tag{4.7}$$

Then, the finite element problem corresponding to the saddle-point problem (4.4) is: Find $(\mathbf{u}_h, \lambda_h) \in V_h \times \Lambda_h$, $u_{2,h} = g_h$ on $\partial\Omega_h$, such that

$$a(\mathbf{u}_h, \mathbf{v}_h) + \hat{b}(\lambda_h, \mathbf{v}_h) = 0 \quad \forall \mathbf{v}_h \in Y_h, \tag{4.8a}$$

$$\hat{b}(\mu_h, \mathbf{u}_h) = 0 \quad \forall \mu_h \in \Lambda_h, \tag{4.8b}$$

where the function $g_h \in V_{2,h}$ is the piecewise linear interpolation of the function $-v_I$, while the bilinear form $\hat{b}(\cdot, \cdot)$ is given by

$$\hat{b}(\mu_h, \mathbf{u}_h) \equiv \int_\Gamma (u_{1,h} - Tu_{2,h}) \overline{\mu}_h \, ds. \tag{4.9}$$

The finite element problem (4.8) leads to a saddle-point linear system of the form

$$\mathbf{Au} \equiv \begin{pmatrix} \mathbf{A}_1 & \mathbf{0} & \mathbf{B}_1^T \\ \mathbf{0} & \mathbf{A}_2 & \mathbf{B}_2^T \\ \mathbf{B}_1 & \mathbf{B}_2 & \mathbf{0} \end{pmatrix} \begin{pmatrix} \mathbf{u}_1 \\ \mathbf{u}_2 \\ \mathbf{u}_\lambda \end{pmatrix} = \begin{pmatrix} \mathbf{0} \\ \mathbf{f} \\ \mathbf{0} \end{pmatrix}, \quad \mathbf{B}_1^T = \begin{pmatrix} \mathbf{0} \\ \mathbf{B}_{1\Gamma}^T \end{pmatrix}, \quad \mathbf{B}_2^T = \begin{pmatrix} \mathbf{B}_{2\Gamma}^T \\ \mathbf{0} \end{pmatrix}, \tag{4.10}$$

where the blocks $\mathbf{A}_1$ and $\mathbf{A}_2$ correspond to the subdomains G_1 and G_2, respectively. The block $\mathbf{A}_1$ is separable, because $G_{1,h}$ is an orthogonal polar mesh. Thus, it is possible to use separation of variables to eliminate all degrees of freedom associated with the nodes outside the interface Γ:

$$\begin{pmatrix} \mathbf{S}_\Gamma & \mathbf{0} & \mathbf{B}_{1\Gamma}^T \\ \mathbf{0} & \mathbf{A}_2 & \mathbf{B}_2^T \\ \mathbf{B}_{1\Gamma} & \mathbf{B}_2 & \mathbf{0} \end{pmatrix} \begin{pmatrix} \mathbf{u}_{1\Gamma} \\ \mathbf{u}_2 \\ \mathbf{u}_\lambda \end{pmatrix} = \begin{pmatrix} \mathbf{0} \\ \mathbf{f} \\ \mathbf{0} \end{pmatrix}, \tag{4.11}$$

where $\mathbf{S}_\Gamma$ is the Schur complement matrix of $\mathbf{A}_1$. The multiplication with the block $\mathbf{S}_\Gamma$ can be performed efficiently using the FFT, because the polar mesh is uniform. Due to the choice of the approximation space for Lagrange multipliers, matrix block $\mathbf{B}_{1\Gamma}^T$ is a symmetric and positive definite tridiagonal matrix.

We precondition the reduced system (4.11) with the matrix $\mathcal{B}$ given by

$$\mathcal{B} \equiv \begin{pmatrix} \mathbf{0} & \mathbf{0} & \mathbf{B}_{1\Gamma}^T \\ \mathbf{0} & \tilde{\mathbf{A}}_2 & \mathbf{B}_2^T \\ \mathbf{B}_{1\Gamma} & \mathbf{B}_2 & \mathbf{0} \end{pmatrix}. \tag{4.12}$$

The subspace of constraints, denoted by S_c, related to the problem (4.11) is defined to be the set of vectors satisfying the last block row; that is,

$$S_c \equiv \left\{ \mathbf{u} = \begin{bmatrix} \mathbf{u}_{\Gamma_1} & \mathbf{u}_2 & \mathbf{u}_\lambda \end{bmatrix}^T : \mathbf{B}_{1\Gamma}\mathbf{u}_{\Gamma_1} + \mathbf{B}_2\mathbf{u}_2 = \mathbf{0} \right\}. \tag{4.13}$$

It is easy to see that when we apply the preconditioner $\mathcal{B}$ to the system (4.11), the subspace of constraints becomes invariant with respect to a preconditioned iterative method of the form (3.4); that is, the condition $\mathbf{u}^{k-1} \in S_c$ implies the condition $\mathbf{u}^k \in S_c$.

The block $\tilde{\mathbf{A}}_2$ is constructed using the fictitious domain approach (see Section 3.3). It is based on an auxiliary boundary value problem of the form (3.8), which in this case is given by

$$\Delta u(\mathbf{x}) + \omega^2 u(\mathbf{x}) = 0, \quad \mathbf{x} \in \hat{\Pi}, \tag{4.14a}$$

$$\frac{\partial u(\mathbf{x})}{\partial \mathbf{n}} - \mathbf{i}\omega u(\mathbf{x}) = 0, \quad \mathbf{x} \in \partial\hat{\Pi}. \tag{4.14b}$$

This problem is discretized using piecewise linear finite elements with mass lumping corresponding to the original triangulated mesh $\hat{\Pi}_h$ from which the locally fitted mesh $G_{2,h}$ was constructed. This procedure results in a separable matrix $\mathbf{B}$.

To obtain a formal representation of the matrix $\tilde{\mathbf{A}}_2$, we write the matrix $\mathbf{B}$ in the following block form, where the second block row corresponds to the degrees of freedoms in $G_{2,h}$:

$$\mathbf{B} \equiv \begin{pmatrix} \hat{\mathbf{A}}_1 & \hat{\mathbf{A}}_{12} \\ \hat{\mathbf{A}}_{21} & \hat{\mathbf{A}}_2 \end{pmatrix}. \tag{4.15}$$

The matrix block $\tilde{\mathbf{A}}_2$ in the preconditioner $\mathcal{B}$ is now given by the Schur complement matrix

$$\tilde{\mathbf{A}}_2 = \hat{\mathbf{A}}_2 - \hat{\mathbf{A}}_{21}\hat{\mathbf{A}}_1^{-1}\hat{\mathbf{A}}_{12}. \tag{4.16}$$

Thus, solution to a linear system of the form $\tilde{\mathbf{A}}_2\mathbf{u}_2 = \mathbf{f}_2$ can be obtained as a restriction of the solution to the larger system

$$\mathbf{B}\begin{pmatrix}\mathbf{u}_1\\ \mathbf{u}_2\end{pmatrix} = \begin{pmatrix}\mathbf{0}\\ \mathbf{f}_2\end{pmatrix}. \tag{4.17}$$

Due to the construction of the matrices $\mathbf{A}_2$ and $\mathbf{B}$, almost all the rows of the matrices $\mathbf{A}_2$ and $\tilde{\mathbf{A}}_2$ coincide. Therefore, the preconditioned iterative procedure for the system (4.11) can be implemented in a low-dimensional subspace.

5. COMPUTATION OF THE RCS

The solution of Eq. (1.1) satisfies the asymptotic representation

$$u(\mathbf{x}) = \frac{e^{\mathbf{i}\omega r}}{\sqrt{r}}F(\hat{\mathbf{x}}, \omega) + \mathcal{O}(r^{-3/2}), \tag{5.1}$$

where $\hat{\mathbf{x}} \equiv \mathbf{x}/r$, and F is an analytic function of its variables called the far-field pattern corresponding to the incident wave and to the scatterer. Using this function, we introduce the radar cross section σ, which describes the asymptotic distribution of the intensity of the scattered wave,

$$\sigma(\hat{\mathbf{x}}, \omega) \equiv 2\pi |F(\hat{\mathbf{x}}, \omega)|^2. \tag{5.2}$$

The radar cross section (RCS) is usually measured in decibel units:

$$RCS(\hat{\mathbf{x}}) = 10 \log_{10} \frac{\sigma(\hat{\mathbf{x}})}{\lambda}, \tag{5.3}$$

where $\lambda \equiv 2\pi/\omega$ denotes the wavelength.

First, we consider the case in which the artificial boundary Γ_∞ is a circle. If the solution is known along a circular boundary Γ, it is possible to derive an analytic representation for the scattered wave in the domain exterior to this boundary. Using this representation we obtain the asymptotic form for the solution,

$$u(r, \theta) \overset{r\to\infty}{\longrightarrow} \frac{1}{\pi}\sqrt{\frac{2}{\pi\omega r}}e^{\mathbf{i}\omega r}\sum_{n=0}^{\infty}{}' \frac{e^{\mathbf{i}(\pi/2)n}}{H_n^{(1)}(\omega R)}\int_0^{2\pi}\cos(n(\theta-\theta'))g(\theta')\,d\theta', \tag{5.4}$$

where g stands for the known numerical solution on the circle Γ. It is then straightforward to see that

$$\frac{\sigma}{\lambda} = \frac{2}{\pi^3}\left|\sum_{n=0}^{\infty}{}' \frac{e^{\mathbf{i}n(\pi/2)}}{H_n^{(1)}(\omega R)}I_n(\theta)\right|^2, \tag{5.5}$$

where

$$I_n(\theta) = \int_0^{2\pi} \cos(n(\theta - \theta'))g(\theta')\,d\theta'. \tag{5.6}$$

The convolution-type integrals I_n can be computed efficiently using the FFT, while the coefficients in the sum of (5.5) are obtained using the recursion formulas for the Hankel functions. The series in (5.5) is terminated after the absolute value of the next term in the series is below the machine precision.

We need to apply another approach, when the artificial boundary is a rectangle instead of a circle. First, we recall that, in the two-dimensional case, the Green function for the Helmholtz operator is given by $G(r) \equiv (\mathbf{i}/4)H_0^{(1)}(r)$. The solution $\mathbf{u}$ of the discrete Helmholtz problem in a rectangle can be expressed as a linear combination of the grid Green functions $\mathbf{g}_k^h$, which are solutions to the discrete problem with the right-hand side equal to the canonical basis vector $\mathbf{e}_k^N$. There is a grid function $\mathbf{b}$ such that the component of $\mathbf{u}$ corresponding to any grid node can be computed using the formula

$$(\mathbf{u})_m = \sum_{k=1}^{N} (\mathbf{b})_k \left(\mathbf{g}_k^h\right)_m, \quad m = 1, \ldots, N. \tag{5.7}$$

For the RCS computation, we need the asymptotic behaviour of the solution. Therefore, we want to extend the discrete solution $\mathbf{u}$ to $\mathbb{R}^2$. By replacing the grid Green function $\mathbf{g}_k^h$ with the continuous Green function we obtain an approximate extension $\tilde{\mathbf{u}}$. The asymptotic behavior of the Hankel functions and the Taylor series for the distance r result in the approximation for the RCS,

$$\sigma(\theta) \approx \frac{1}{4\omega} \left| \sum_k (\mathbf{b})_k e^{-\mathbf{i}\omega h(k_x \cos\theta + k_y \sin\theta)} \right|^2, \tag{5.8}$$

where k_x and k_y are the row and column numbers of the node k in the rectangular grid. This formula can be used in our algorithm to compute the RCS, because the values $(\mathbf{b})_k$ are known after the iterative solution.

6. TEST EXAMPLES

Each test example is described by the obstacle Ω, the wavenumber ω, and the angle ϕ between the positive x–axis and the incident vector $\boldsymbol{\omega}$. In the first test case, the obstacle Ω was a disc with radius $r_0 = 0.375$ centered at the point (0.5, 0) on the x–axis. The angle of incidence and the wave number were given by $\phi = 0^\circ$ and $\omega = 8\pi$, and, thus, the wavelength λ was $\frac{1}{4}$. In this case, the known analytic solution was used as a reference solution. The circle was shifted, because otherwise a direct solver could have been used in the case with a polar mesh.

In the second test series, the obstacle Ω was an ellipse the foci of which were the points $(\pm c, 0)$ on the x–axis. The boundary of an ellipse is given by the equation

$$\frac{x^2}{c^2 \cosh^2 \xi_0} + \frac{y^2}{c^2 \sinh^2 \xi_0} = 1, \tag{6.1}$$

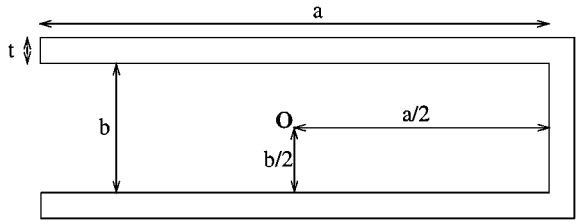

FIG. 4. The dimensions of the semi-open cavity.

where the parameter ξ_0 was chosen such that the aspect ratio of the ellipse was 14. The angle of incidence was $\phi = 30^\circ$, while the wave number was given by $\omega = 10\pi/c$, where the parameter c was chosen to be 0.6. Thus, there were approximately 10.03 wavelengths along the major axis of the ellipse. In the case of an elliptical scatterer, the analytic solution can be represented in terms of Mathieu functions (see [28]). We computed the analytic solution by using the known representation, and thereby obtained a reliable reference solution for our numerical experiments.

In the third test example, the scatterer Ω was the semi-open cavity illustrated in Fig. 4 with the parameters $a = 4$, $b = 1$, and $t = 0.2$. The wave number was chosen to be $\omega = 4\pi$ leading to the wavelength $\lambda = \frac{1}{2}$, and the angle of incidence was $\phi = 0^\circ$. Here, the analytic solution is not known, and in order to obtain a reference solution we solved the problem in polar coordinates using the exact nonreflecting boundary condition (2.6) and high discretization accuracy.

The errors were computed by comparing the radar cross section (RCS) of the numerical solution and the reference solution. The approximation error was measured with the maximum norm (L_∞–norm) given by

$$\| f^* - f \|_\infty \equiv \max_{x \in [0, 2\pi]} | f^*(x) - f(x) |, \tag{6.2}$$

where f and f^* are the approximate and accurate RCSs, respectively.

We made additional tests with two high-frequency problems in which the scatterers were the ellipse and the semi-open cavity introduced above. In the case with the ellipse, we used the incident angle $\phi = 30^\circ$ and the wave number $\omega = 50\pi$, which corresponds to the wavelength $\lambda = \frac{1}{25}$. Thus, there were approximately 30 wavelengths along the major axis. With the semi-open cavity, the incident angle and the wave number were $\phi = 30^\circ$ and $\omega = 10\pi$, which leads to the wavelength $\lambda = \frac{1}{5}$.

7. NUMERICAL EXPERIMENTS

In this section, we present results of numerical experiments with the fictitious domain methods considered in Section 3 and with the domain decomposition approach considered in Section 4. One of the aims of our numerical experiments was to demonstrate that the approximate boundary value problem with a rectangular artificial boundary and the nonreflecting boundary condition (2.4) does not provide sufficiently accurate approximation to the original problem (1.1). There exists a lower bound for the error of approximation independent of the size of the rectangle and accuracy of discretization. Another aim was to compare the different solvers in terms of efficiency. We chose some accuracy levels and determined the minimum distance between the obstacle and the artificial boundary and the maximum grid

step size required to reach this accuracy. Then, we compared the numbers of iterations and the CPU time consumptions of the different methods.

As our iterative solution method, we applied the preconditioned GMRES method without restarting, which was continued until the relative norm of the residual $\mathbf{r}^k$ had decreased by a given factor ε, that is, when the criterion $\|\mathbf{r}^k\|_2 \le \varepsilon\|\mathbf{r}^0\|_2$ was satisfied. Throughout the tests in this section, we used the value 10^{-6} for the factor ε. The initial approximation $\mathbf{u}^0$ for the iterative method was always chosen to be the zero vector. This choice allowed us to implement the iterative procedure in the subspace $\text{im}\,\hat{\mathbf{A}} \cap \text{im}(\hat{\mathbf{A}} - \mathbf{B})$, because the right-hand side vector $\hat{\mathbf{f}}$ belongs to this space.

The following notations are used throughout this section. All the tests were performed on an HP9000/J280 workstation (180 MHz PA8000 CPU, 256 MB RAM):

d	the shortest distance between the scatterer and the artificial boundary (in terms of the wavelength).
N	dimension of the reduced linear system.
N_{ss}	dimension of the subspace $\text{im}\,\mathcal{A} \cap \text{im}(\mathcal{A} - \mathcal{B})$.
L	number of nodes per wavelength.
D	characteristic size of the scatterer.
ite	total number of iterations
T_{prec}	CPU time (in seconds) for solving one linear system with the preconditioner.
T_{ite}	CPU time for the iterative solution.

The fictitious domain methods working with polar and cartesian locally fitted meshes are referred to as the **Polar**- and **Cart**-methods, respectively. The method coupling the two mesh systems is referred to as the **Coup**-method. Each polar locally fitted mesh is constructed from a uniform rectangular polar mesh Π_h with the grid step sizes Δr and $\Delta\theta$ in the coordinate directions r and θ, respectively. The grid step sizes are given by the relations $\Delta r = \lambda/L$ and $\Delta\theta = \Delta r/R_0$, where R_0 is the minimal radius of a circle circumscribing the scatterer.

In the **Polar**-method and the **Coup**-method, we have a uniform orthogonal polar mesh outside some circle. As pointed out in Section 4, the matrix block corresponding to this part of the mesh can be eliminated efficiently by using the separation of variables, which motivates the use of a polar mesh outside a given circle. When the DtN condition (2.6) is used in the **Coup**-method, the polar mesh is introduced only on the subdomain boundary Γ and the elimination procedure is not needed.

In the numerical tests, the accuracy of the different methods was studied by computing and comparing the radar cross sections of the numerical solutions. For this purpose, we chose three different accuracy levels: $\varepsilon_1 = 4 \times 10^{-1}$, $\varepsilon_2 = 2 \times 10^{-1}$, and $\varepsilon_3 = 2 \times 10^{-2}$. After selecting a particular accuracy level, we chose some relatively small artificial domain Π and started to gradually increase the number of nodes per wavelength. If we use a local nonreflecting boundary condition and fix the size of the boundary Γ_∞, there is a lower bound for the accuracy independent of the mesh step size. We refined the mesh until this accuracy was obtained, and then enlarged the domain Π by a small amount. After the enlargement, we again performed the mesh refinement to reach the maximum accuracy for that particular Π. This procedure was repeated until the error was reduced below the chosen accuracy level. The same procedure was done with all the local nonreflecting boundary conditions considered in Section 2.

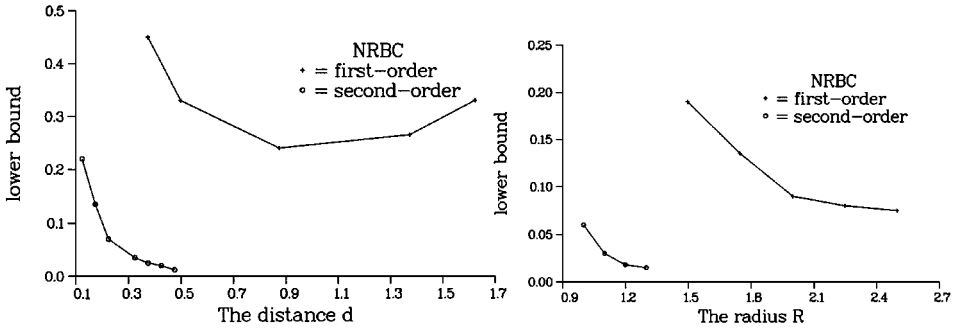

FIG. 5. The dependence of the lower bound for the error on the size of the artificial domain. On the left, for a rectangular boundary and on the right, for a circular boundary.

The results of the experiments with the first test case are illustrated in Fig. 5. The two figures depict the improvement in accuracy as the distance of the artificial boundary Γ_∞ from the obstacle boundary is increased. Figure 5 shows that with the **Cart**-method using the first-order boundary condition (2.4) the error ceases to decrease as the distance d of the artificial boundary from the obstacle is increased. This result confirms that there exists a lower bound for the approximation error independent of the size of the artificial domain. The figure on the right is obtained by using a circular boundary and the boundary conditions (2.2) and (2.3). We see that the accuracy of the first-order boundary condition (2.2) improves when the radius of the boundary Γ_∞ is increased and the error is not bounded from below. Furthermore, the experiment shows clearly the improvement in accuracy provided by the second-order conditions (2.3) and (2.5).

In our tests with the exact boundary condition, we used the value $K = n_2$ to truncate the infinite series in (2.6), that is, K equals the number of nodes in the angular direction in the polar mesh. We fixed the radius of the artificial boundary at the value $R = 1.0$ and gradually increased the number of nodes per wavelength. A graph of the maximum error in the RCS versus the number of nodes per wavelength is given in Fig. 6, which shows how the error decreased and no lower bound emerged. The tightest accuracy level ε_3 was easily obtained and surpassed.

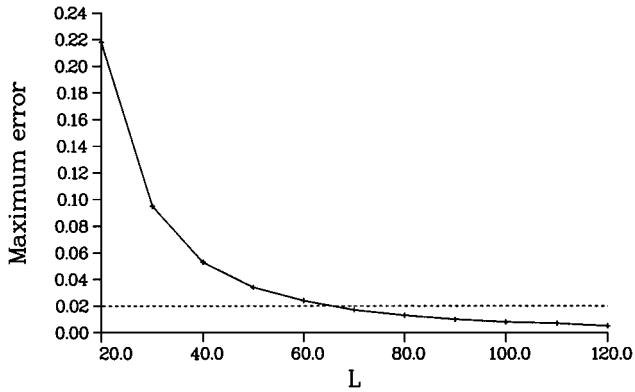

FIG. 6. The maximum error versus the discretization accuracy with the exact boundary condition (2.6).

TABLE I
The Parameters for Four Different Methods Required to Reach the Error Level ε_3 with the First Test Obstacle

	d	L	N_{ss}	N	ite	T_{prec}	T_{ite}
Polar, 2nd	1.3λ	75	2926	5.7e5	44	2.9	126
Coup, 2nd	1.7λ	80	10218	4.4e5	46	2.2	107
Polar, DtN	0.5λ	70	2737	4.3e5	41	2.3	95
Coup, DtN	0.5λ	75	9566	3.8e5	47	2.0	97

Using the first test example, we compared the **Polar**-method and the **Coup**-method with different boundary conditions both in terms of memory consumption and CPU time usage. We searched for the parameters R and L leading to an error below the level ε_3. The results are presented in Table I, and we can see that, in this particular example, the performance of the two methods is practically the same. The memory consumption is significantly lower with the **Polar**-method, because the obstacle Ω is shifted away from the origin of coordinates. This makes the polar mesh around the obstacle sparser and reduces the dimension of the arising subspace.

In the second test case (Fig. 7), we searched, with five different methods, for the minimum size of the artificial boundary and minimum number of nodes per wavelength required to reach the second error level ε_2. The results are presented in Table II, and they indicate that the **Cart**-method with the second-order nonreflecting boundary condition is the most efficient one among the five methods. This is due to the small dimension of the subspace in which the iterative solution is computed. Here, the coupling of polar and cartesian meshes provides clear improvement to the case with purely polar meshes. The surface of the thin ellipse goes near the origin of coordinates, and, therefore, the polar mesh around the scatterer becomes very dense thereby increasing the dimension of the subspace in the **Polar**-method. Thus, the ratio between the values N_{ss} in **Coup**-method and in **Polar**-method is reduced, compared to the case with the circle, and the CPU time consumption of the **Coup**-method becomes lower, compared to the **Polar**-method.

In the third test case (Fig. 8), the reference solution was computed with the **Polar**-method using the exact boundary condition (2.6) and 120 nodes per wavelength. We searched for the parameters d and L to reach the error level ε_1 with respect to the maximum norm. The results are presented in Table III, and again, the **Cart**-method gives the best results. The numerical results suggest that the reference solution obtained with the **Polar**-method is not

TABLE II
Results with the Thin Ellipse and Wavelength 3/25

	d	L	N_{ss}	N	ite	T_{prec}	T_{ite}
Cart, 2nd	6.0λ	80	3280	1.8e6	63	2.9	197
Polar, 2nd	3.5λ	80	8014	1.0e6	69	5.0	368
Polar, DtN	0.2λ	80	8014	1.0e6	69	5.1	375
Coup, 2nd	3.5λ	80	14322	7.4e5	74	3.0	238
Coup, DtN	0.2λ	80	14322	7.4e5	74	2.8	221

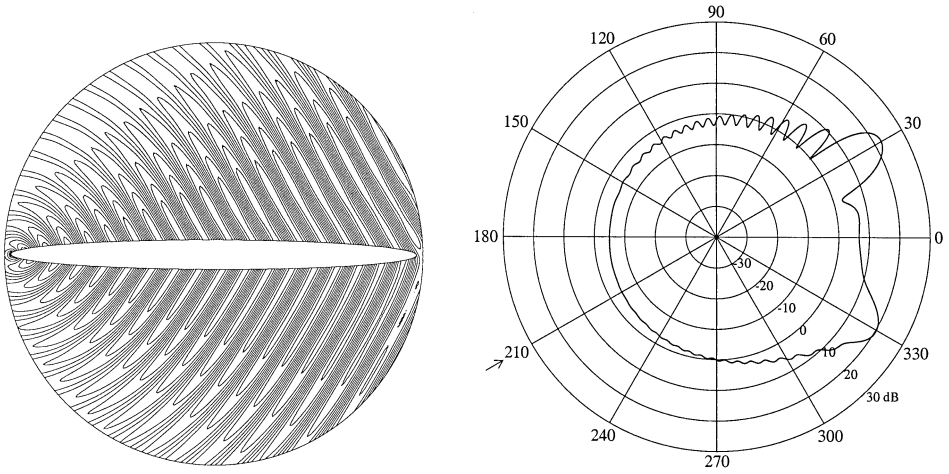

FIG. 7. The real part of the scattered field and the related RCS for the ellipse.

quite reliable, since the number of nodes per wavelength required by the error level ε_1 is smaller with the **Polar**-method than with the other methods.

We made experiments also with higher frequencies using the ellipse and the semi-open cavity as the scatterers. In the case with the ellipse, we chose the wave number ω such that there were 30 wavelengths between the foci of the ellipse. With the semi-open cavity, the number of wavelengths along the obstacle was 20. The solutions were computed using the **Cart**-method with the second-order nonreflecting boundary condition and the **Coup**-method with the exact boundary condition.

We fixed the discretization resolution to be 30 nodes per wavelength. The rectangular artificial infinity in **Cart**-method was chosen by increasing the distance d between the ellipse and the artificial boundary until the resulting error was of the same order of magnitude as the error of the **Coup**-method with the exact boundary condition. The same distance d was used in the test with the cavity.

Again, **Cart**-method with the second-order boundary condition surpasses **Coup**-method with a clear marginal in computational performance, whereas the accuracy of the two methods is approximately the same. The radar cross sections for the two test problems are illustrated in Fig. 9. In the graph related to the semi-open cavity, there are two curves corresponding to the two solvers. The solid curve corresponds to the **Coup**-method and the dashed curve to the **Cart**-method.

TABLE III
Results with the Semi-Open Cavity and Wavelength $\frac{1}{2}$

	d	L	N_{ss}	N	ite	T_{prec}	T_{ite}
Cart, 2nd	4.5λ	70	5381	1.0e6	100	1.9	250
Polar, 2nd	2.5λ	60	9451	5.0e5	120	4.1	508
Polar, DtN	0.3λ	60	9451	5.0e5	119	3.9	495
Coup, 2nd	2.5λ	70	14202	4.8e5	138	3.1	438
Coup, DtN	0.3λ	70	14202	4.8e5	135	2.9	410

TABLE IV
Results with the High-Frequency Problems

	d	L	N_{ss}	N	ite	T_{prec}	T_{ite}
Ellipse							
Cart, 2nd	7.0λ	30	3688	6.4e5	152	1.3	240
Coup, DtN	0.3λ	30	15988	8.8e5	159	4.0	695
Semi-open cavity							
Cart, 2nd	7.0λ	30	5765	6.6e5	260	1.4	445
Coup, DtN	0.3λ	30	15190	5.2e5	264	2.1	745

8. CONCLUSIONS

The approximation accuracy of the first-order boundary condition (2.4) on a rectangular boundary was demonstrated to be insufficient. This condition leads to spurious reflection of waves as pointed out in many papers before (see, e.g., [17]). With the second-order boundary condition (2.5), however, it is possible to reach high accuracy.

On a circular artificial boundary, the numerical results recommend the use of the exact boundary condition (2.6). First, it leads to higher accuracy than the local conditions and allows one to position the artificial boundary as close to the obstacle as possible. Second, the computational cost of using the exact boundary condition in the fictitious domain method is the same as with the local conditions. Although the matrix block associated with the nonlocal boundary condition is dense, it has a circulant structure and can thus be diagonalized with the standard Fourier matrix. Therefore, FFT-based fast solvers can be applied to the linear systems with the corresponding separable preconditioner.

We were able to reach improvement in the computational performance by replacing a polar locally fitted mesh with a coupled polar/cartesian mesh as was shown by the test case with the ellipse. Furthermore, the coupling approach can be readily used in problems with piecewise constant coefficients, and it provides an attractive alternative to treat exterior problems with material inhomogenities in some neighbourhood of the obstacle.

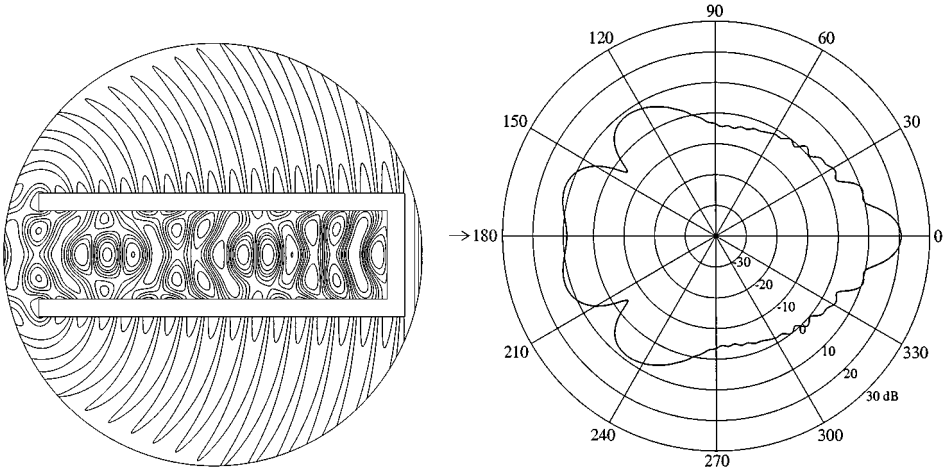

FIG. 8. The real part of the scattered field for the semi-open cavity and the resulting RCS.

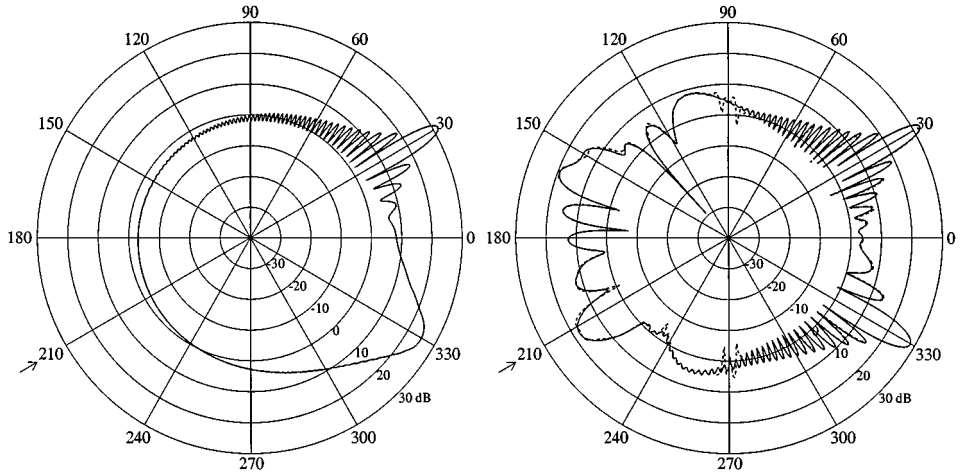

FIG. 9. The radar cross sections of the ellipse (on the left) and the semi-open cavity (on the right) in the high-frequency cases.

One drawback of the coupling procedure is that the mesh is fitted, in addition to the obstacle surface, also to the interface Γ, which increases the dimension of the subspace in which the iterative method operates. The **Coup**-method is not flexible with respect to the aspect ratio of the scatterer, since the interface Γ needs to be a circle. This restriction is especially important in the case when the scatterer is very thin (for example, a thin ellipse or an airfoil).

According to our tests, the **Cart**-method, together with the second-order boundary condition (2.5) is the most efficient method among the ones considered here, although the differences are not significant. In this method, the subspace for the iterative procedure is associated only with the nodes in the neighbourhood of the scatterer and, therefore, its dimension is considerably lower than in the case with the coupled mesh. Moreover, in the **Cart**-method we have better possibilities to adapt the artificial boundary to the geometry of the obstacle, which reduces the dimension of the total problem.

The numerical results suggest that the distance of the rectangular artificial boundary from the scatterer has to be six to seven wavelengths in order to obtain as accurate solutions as are obtained using the exact boundary condition on a circular boundary. Moreover, it is not clear what the effect is on accuracy, if the geometry of the scatterer becomes more complex.

REFERENCES

1. W. Jäger, Zur Theorie der Schwingungsgleichung mit variablen Koeffizienten in Aussengebieten, *Math. Z.* **102** (1967).
2. V. Rokhlin, Rapid solution of integral equations of scattering theory in two dimensions, *J. Comput. Phys.* **86**, 2 (1990).
3. G. I. Marchuk, Yu. A. Kuznetsov, and A. M. Matsokin, Fictitious domain and domain decomposition methods, *Soviet J. Numer. Anal. Math. Modelling* **1**, 3 (1986).
4. T. Rossi, *Fictitious Domain Methods with Separable Preconditioners*, Ph.D. thesis, University of Jyväskylä, Finland, 1995.
5. A. Bespalov, *Application of Fictitious Domain Method to the Solution of the Helmholtz Equation in Unbounded Domain*, Rapport de Recherche 1797, INRIA, France, 1992.

6. A. Bespalov, Y. Kuznetsov, O. Pironneau, and M.-G. Vallet, Fictitious domains with separable preconditioners versus unstructured adapted meshes, *IMPACT Comp. Sci. Eng.* **4** (1992).
7. Yu. A. Kuznetsov, Matrix computational processes in subspaces, in *Comput. Math. in Appl. Sci. and Eng. VI*, edited by R. Glowinski and J. L. Lions (North Holland, Amsterdam, 1984), p. 15.
8. Yu. A. Kuznetsov and K. Lipnikov, A fictitious domain method for solving the Helmholtz wave equation in unbounded domains, in *Numer. Meth. Math. Modelling*, edited by Yu. A. Kuznetsov (Institute of Numerical Mathematics of Russian Academy of Sciences, Moscow, 1992), p. 56 [Russian]
9. Yu. A. Kuznetsov and K. Lipnikov, *On the Application of Fictitious Domain and Domain Decomposition Methods for Scattering Problems on Cray Y–MP C98*, Technical Report 9557, Department of Mathematics, University of Nijmegen, The Netherlands, 1995.
10. Yu. A. Kuznetsov and A. M. Matsokin, On partial solution of systems of linear algebraic equations, in *Vychislitel'nye Metody Lineinoy Algebry (Computational Methods of Linear Algebra)*, edited by G. I. Marchuk (Vychisl. Tsentr Sib. Otdel. Akad. Nauk SSSR, Novosibirsk, 1978), p. 62.
11. E. Heikkola and Yu. A. Kuznetsov, *Finite Element Method on Nonmatching Meshes for the Helmholtz Equation*, Report 18/1995, Laboratory of Scientific Computing, Department of Mathematics, University of Jyväskylä, Finland, 1995.
12. E. Heikkola, *Domain Decomposition Method with Nonmatching Grids for Acoustic Scattering Problems*, Ph.D. thesis, University of Jyväskylä, Finland, 1997.
13. O. G. Ernst, A finite-element capacitance matrix method for exterior Helmholtz problems, *Numer. Math.* **75** (1996).
14. C. I. Goldstein, The finite element method with non-uniform mesh sizes applied to the exterior Helmholtz problem, *Numer. Math.* **38**, 61 (1981).
15. C. I. Goldstein, The solution of exterior interface problems using a variational method with Lagrange multipliers, *J. Math. Anal. Appl.* **97**, 480 (1983).
16. F. R. Cooray and G. I. Costache, An overview of the absorbing boundary conditions, *J. Electromagn. Waves Appl.* **5**, 1041 (1991).
17. D. Givoli, Non-reflecting boundary conditions, *J. Comput. Phys.* **94**, 1 (1991).
18. A. Bayliss, M. Gunzburger, and E. Turkel, Boundary conditions for the numerical solution of elliptic equations in exterior regions, *SIAM J. Appl. Math.* **42**, 430 (1982).
19. B. Engquist and A. Majda, Absorbing boundary conditions for the numerical simulation of waves, *Math. Comp.* **31**, 629 (1977).
20. B. Engquist and A. Majda, Radiation boundary conditions for acoustic and elastic wave calculations, *Comm. Pure Appl. Math.* **32**, 313 (1979).
21. L. Halpern and J. Rauch, Error analysis for the absorbing boundary conditions, *Numer. Math.* **51**, 459 (1987).
22. A. Bamberger, P. Joly, and J. E. Roberts, Second-order absorbing boundary conditions for the wave equation: a solution for the corner problem, *SIAM J. Numer. Anal.* **27**, 323 (1990).
23. R. C. MacCamy and S. P. Marin, A finite element method for exterior interface problems, *Int. J. Math. Math. Sci.* **3**, 2 (1980).
24. J. B. Keller and D. Givoli, Exact non-reflecting boundary conditions, *J. Comput. Phys.* **82**, 172 (1989).
25. I. Harari and T. J. R. Hughes, Analysis of continuous formulations underlying the computation of time-harmonic acoustics in exterior domains, *Comput. Methods Appl. Mech. Eng.* **97**, 103 (1992).
26. F. Ihlenburg and I. Babuška, Finite element solution to the Helmholtz equation with high wave number. Part I. the h–version of the FEM, *Comput. Math. Appl.* **30**, 9 (1995).
27. A. Banegas, Fast Poisson solvers for problems with sparsity, *Math. Comp.* **32**, 441 (1978).
28. N. W. McLachlan, *Theory and Application of Mathieu Functions* (Dover, New York, 1964).